Joint Optimization of Transmit Power and Trajectory for UAV-Enabled Data Collection With Dynamic Constraints

Hongyun Zhang, Bin Li*, *Senior Member, IEEE,* Yue Rong, *Senior Member, IEEE,*
Yong Zeng, *Senior Member, IEEE,* Rui Zhang, *Fellow, IEEE*

Abstract—The unmanned aerial vehicle (UAV)-enabled data collection system with a rotary-wing UAV and multiple ground nodes (GNs) is investigated in this paper. The average transmission data rate is maximized through the coordinated optimization of the GNs' transmit power and the UAV's trajectory. In particular, the UAV dynamic constraints and physical constraints are imposed. The UAV dynamics, which are governed by a group of differential equations, are usually ignored in existing works. As a consequence, the planned trajectory cannot be fully tracked by the controller in real world applications, which could lead to severe performance degradation. Thus, a control-based method is devised to address this issue. Specifically, by adopting the state-space model from control theory, the data collection problem is established as a dynamic optimization problem subject to state constraints, in which both of the decision variables and constraints are infinite-dimensional in nature. The key idea of the solution method is to convert the infinite-dimensional dynamic program into a finite-dimensional static nonlinear problem. This is achieved by deriving the required gradients of the dynamic optimization problem based on the control parametrization scheme and an exact penalty function method. The effectiveness and superiority of the proposed design are validated via numerical experiments.

Index Terms—UAV-enabled data collection, trajectory optimization, power allocation, control parametrization.

I. INTRODUCTION

Drones, also known as unmanned aerial vehicles (UAVs), have been widely investigated as aerial platforms in new generation wireless networks. Typical examples include mobile aerial base stations (BSs) [1]–[4], mobile data gathering equipment [5]–[8], aerial monitors [9], [10], aerial communications relays [11]–[13], cellular-connected users [14]–[16], and mobile edge computing (MEC) servers [17]–[19]. Due to their high mobility and on-demand deployment characteristics, UAVs are envisioned to play a significant role in wireless sensor networks (WSNs). Utilizing UAVs for collecting data from distributed sensors offers great flexibility and efficiency compared to using terrestrial BSs. Moreover, UAV-assisted data collection is able to be utilized in complex terrains and the communication performance can be improved by taking advantage of the strong direct link between the ground terminal and the UAV.

As a key technique for UAV-enabled communications, trajectory optimization for UAV-assisted data collection has been intensively investigated [4], [8], [20]–[26]. In [4], the throughput maximization problem is studied by optimizing the flying trajectory, the transmit power of the UAV and the source. A successive convex optimization based solution method is developed and implemented in an alternating manner. The UAV-enabled data collection problem is studied by designing the trajectory to maximize energy-efficiency in [20]. A solution method is developed based on the state-space model and successive convex approximation (SCA) technique. In [21], data collection from multiple sensor nodes (SNs) with a UAV is considered. The problem of minimizing task execution time by optimally designing the UAV flight trajectory point and the SN assignment, which is solved by a convex approximation technique. The UAV-assisted data acquisition problem with time-constrained internet of things (IoT) devices is studied in [22], where the design of radio resource allocation and flying trajectory aims to maximize the total number of served IoT devices. A branch and bound based method is proposed and a low-complexity sub-optimal solution method is also developed based on the well-known SCA technique.

Considering the UAV-enabled data collection problem for WSN in [23], an offline joint design scheme for the flying trajectory and the transmit power is proposed for improving the average throughput and reducing the outage probability. Meanwhile, a convex theory based method is developed by finding the UAV flying pattern through problem relaxation. In [24], the UAV-enabled data collection problem for multiple SNs is investigated. The age of information (AoI) of SNs is optimized by jointly designing the discrete flight trajectory and the SN associations. A two-step method is developed by optimizing the SN association and flight trajectory at each

*Corresponding author

H. Zhang and B. Li are with School of Aeronautics and Astronautics, Sichuan University, Chengdu, Sichuan 610065, China, e-mail: zhanghongyun1@stu.scu.edu.cn; bin.li@scu.edu.cn.

Y. Rong is with the School of Electrical Engineering, Computing and Mathematical Sciences, Curtin University, GPO Box U1987, Perth, WA 6845, Australia, e-mail: y.rong@curtin.edu.au

Y. Zeng is with National Mobile Communications Research Laboratory, Southeast University, Nanjing, Jiangsu 210096, China, and also with the Purple Mountain Laboratories, Nanjing 211111, China, e-mail: yong_zeng@seu.edu.cn.

R. Zhang is with School of Science and Engineering, Shenzhen Research Institute of Big Data, The Chinese University of Hong Kong, Shenzhen, Guangdong 518172, China (e-mail: rzhang@cuhk.edu.cn). He is also with the Department of Electrical and Computer Engineering, National University of Singapore, Singapore 117583 (e-mail: elezhang@nus.edu.sg).

step. In [25], a reinforcement learning based method is developed for optimizing the flight trajectory and the throughput of the UAV-enabled IoT system. In [26], energy efficiency maximization for the cognitive UAV-assisted traffic offloading is addressed. The flying trajectory and the communication of cognitive UAV are obtained by a learning-based method with the uncertain environmental information. In [8], the data collection case for multiple UAVs from heterogeneous users is investigated. A joint design of UAV trajectory and user associations is proposed to achieve optimization of multiple metrics simultaneously. Inspired by game theory and reinforcement learning, an effective computational method is proposed.

As far as we know, most existing works [4], [8], [20]–[26] only consider the flight speed or acceleration constraints of the UAV, but do not analyze its motion capability based on the forces imposed on it, that is, they ignore the dynamic constraints of the UAV. In addition, the optimized trajectories obtained are a series of piece-wise line segments with the assumption that the UAV speed and acceleration are constant during each time interval. However, a UAV is a complex dynamic system governed by a group of differential equations including the kinematic and the dynamic equations [27]. The kinematic equations describe the motion of a UAV, while the relationships between the UAV motion and the forces applied to it are revealed by the dynamic equations. If the UAV dynamic constraints are ignored in the trajectory design, the planned trajectory may not be well-tracked by the controller in engineering practice, which may lead to severe performance degradation.

Motivated by the above discussion, the design of GN transmit power and flight trajectory for UAV-assisted data collection is investigated. In addition, the UAV's dynamic constraints and physical constraints are considered. More specifically, a rotary-wing UAV is sent out to gather data from multiple GNs. The average transmit data rate is maximized by jointly designing the transmit power of each GN and the flying trajectory.

The state-space model from [28] is adopted to tackle the challenges from the dynamic constraints. With the state-space model, the initial optimization problem is transformed into a dynamic program subject to state constraints. The key idea of this work is to derive the gradient formulas and convert the dynamic program into a static nonlinear problem. Thus, we propose a control-based design by integrating the control parametrization technique and the exact penalty function method. Specifically, the infinite-dimensional decision variables are transformed into finite-dimensional ones by the control parametrization scheme. Moreover, the infinite-dimensional state constraints are addressed through the exact penalty function method. Meanwhile, the existing numerical algorithms, such as sequential quadratic programming (SQP), can be exploited to yield a high-quality solution of the converted static nonlinear problem.

It is worth emphasizing that the control parametrization method is a general and effective framework which is capable of solving a range of dynamic optimization problems. For different types of problems, different problem conversion techniques and gradient formulas can be derived under this framework. Thus, unlike the control-based design for the single-node communication problem discussed in our previous work [29], the control parametrization method based design is proposed for the multi-node data collection problem in this work. Furthermore, a joint optimization scheme for the UAV trajectory and the GN transmit power is developed in this work, whereas only the trajectory was optimized in [29]. In addition, the dynamic model with only translational motion considered in this paper is a simplified version of [29]. This simplification helps ease the computational burden of the algorithm and facilitates the on-board implementation. Moreover, physical constraints are dealt with an exact penalty function method in this work, instead of the constraint transcription method used in [29].

The contributions of this work have been summarized as follows:

- Compared with existing works on UAV-enabled data collection [4], [8], [20]–[26], the UAV dynamic constraints are considered in this work, which gives rise to a more tractable trajectory for the UAV and less performance degradation.
- Compared with [29], the computational overhead of this work is reduced by introducing a simplified UAV model, which achieves a good trade-off between the complexity and performance.
- A control-based design is developed by adopting the state-space model. This approach converts the dynamic optimization problem into a static nonlinear program. Additionally, the necessary gradient formulas are derived.

The rest of this paper is organized as follows. In Section II, we present the system description with dynamic constraints and formulate the dynamic optimization problem to maximize the average data rate. In Section III, the solution method, which is designed based on the control parametrization scheme and an exact penalty function method, is proposed. Section IV evaluates the effectiveness of this method through several numerical examples. Finally, we conclude this article in Section V.
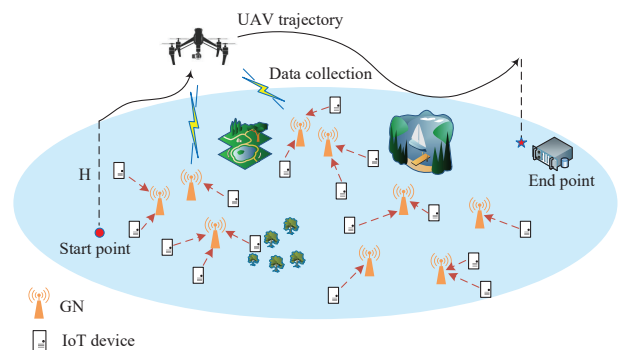
II. SYSTEM MODEL AND PROBLEM FORMULATION

Fig. 1: The UAV-enabled data collection system.

As shown in Fig. 1, the system which consists of a rotary-wing UAV, M GNs, and multiple IoT devices, is considered.

TABLE I: Important Notations

|	
m_u	Weight of UAV (kg)
g	Gravitational acceleration (m/s^2)
V	UAV speed (m/s)
F	Engine thrust (N)
D	Drag force (N)
α	Attack angle (rad)
ψ	Heading angle (rad)
C_d	Fuselage drag coefficient
β_0	Channel power at the reference distance of 1 meter
ι	Path loss exponent
ϕ_m	Channel phase shift from the mth GN to UAV
P_m	Transmit power (W) of the mth GN
φ_m	Signal phase of the mth GN
P_m^{ave}	Maximum average transmit power of the mth GN (W)
z	Additive white Gaussian noise
σ^2	Noise power (W)
B	Bandwidth (MHz)
V_{max}	Maximum safe flying airspeed (m/s)
α_{max}	Maximum safe flying attack angle (rad)
ψ_{max}	Maximum safe flying heading angle (rad)
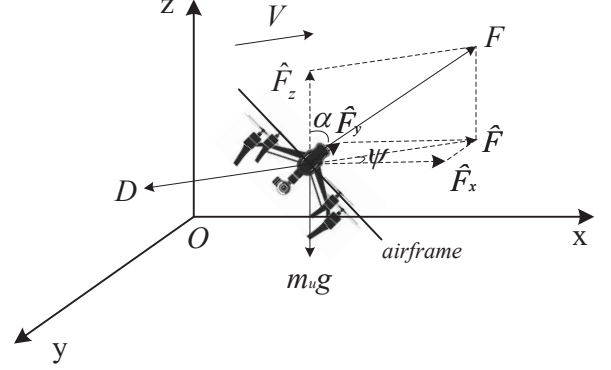
Fig. 2: The forces on a UAV with rotary wings.

Data collected by IoT devices are first sent to a nearby GN. It is assumed that orthogonal transmission is employed in the uplink and simultaneous data upload from all of the GNs to the UAV are allowed. The GNs are randomly distributed with index $\mathcal{M} \triangleq \{1, 2, \ldots, M\}$. The coordinate for the mth GN is denoted as $(\boldsymbol{o}_m^\top, 0) = (x_m, y_m, 0)$, where $\boldsymbol{o}_m$ denotes the horizontal location of the GN and $(\cdot)^\top$ stands for the transpose operation. Limited by the battery capacity, the UAV is supposed to fly from a start point to an end point within a fixed time duration $\mathcal{T} \triangleq [0, T]$, and it gathers data from multiple GNs simultaneously during flight. Furthermore, the UAV is assumed to fly within a fixed horizontal plane and the altitude is H. The objective of this work is to jointly design the flying trajectory and the transmit power such that the average data rate is maximized, while the transmit power constraints of GNs, the dynamic constraints and the physical constraints of UAV are satisfied. Note that some important notations are described in Table I for readers' convenience.

A. Dynamic Model of Rotary-Wing UAV

As depicted in Fig. 2, the forces on a UAV with rotary wings during level flight at speed V are shown, where F represents the thrust force, D represents the drag force, $\hat{F}$ represents the projection of F onto the horizontal plane. Let $\boldsymbol{q}(\tau) = (x(\tau), y(\tau))^\top$ be the coordinates of the UAV at $\tau \in \mathcal{T}$.

According to [30], [31], the relationship between D and V is given below:

$$D = C_d V^2, \tag{1}$$

where C_d is defined in Table I.

Let a_x, a_y and a_z be the accelerated speed on x, y and z axis, respectively. According to Newton's second law, we have

$$\begin{cases} m_u a_x = \hat{F}_x - \text{sign}(D_x)D_x, \\ m_u a_y = \hat{F}_y - \text{sign}(D_y)D_y, \\ m_u a_z = \hat{F}_z - \text{sign}(D_z)D_z - m_u g, \end{cases} \tag{2}$$

where $\text{sign}(x)$ stands for the sign of x, $\hat{F}_x$, $\hat{F}_y$, and $\hat{F}_z$ are the projections of F on x, y and z axis, respectively, given by

$$\begin{aligned} \hat{F}_x &= F \sin \alpha \cos \psi, \\ \hat{F}_y &= F \sin \alpha \sin \psi, \\ \hat{F}_z &= F \cos \alpha, \end{aligned} \tag{3}$$

and D_x, D_y, D_z are the projections of D on x, y and z axis, respectively. According to (1), D_x, D_y, D_z can be written as

$$D_x = C_d v_x^2, D_y = C_d v_y^2, D_z = C_d v_z^2, \tag{4}$$

where v_x, v_y and v_z represent the velocity on the x axis, y axis and z axis, respectively. By substituting (3) and (4) into (2), it yields

$$\begin{cases} m_u a_x = F \sin \alpha \cos \psi - \text{sign}(v_x)C_d v_x^2, \\ m_u a_y = F \sin \alpha \sin \psi - \text{sign}(v_y)C_d v_y^2, \\ m_u a_z = F \cos \alpha - \text{sign}(v_z)C_d v_z^2 - m_u g. \end{cases} \tag{5}$$

Since the UAV is moving on a horizontal plane, then $a_z = 0$ and $v_z = 0$. Thus, from (5), it follows that

$$F = m_u g / \cos \alpha. \tag{6}$$

Then, we substitute (6) into (5), which gives

$$\begin{cases} a_x = g \tan \alpha \cos \psi - \text{sign}(v_x)\dfrac{C_d}{m_u} v_x^2, \\ a_y = g \tan \alpha \sin \psi - \text{sign}(v_y)\dfrac{C_d}{m_u} v_y^2. \end{cases} \tag{7}$$

Therefore, the following dynamic model (8)[1] can be obtained by noting the fact that $\dot{v}_x = a_x$ and $\dot{v}_y = a_y$:

---

[1] The dynamic model (8) is a simplified version of [29]. In [29], a 6 degree of freedom (6-DoF) model is considered, which implies that both translation and rotational motion are considered. In (8), only the translation motion is addressed, which is a 3 degree of freedom (3-DoF) model. In addition, since level flight is considered, a 2-dimensional model is adopted here. Although the dynamic model is simplified, the forces on the UAV are clearly revealed in (8). Moreover, the computational overhead is highly reduced since the 12-dimensional differential equations in [29] are reduced to a 4-dimensional one as illustrated in (8).

$$
\begin{cases}
\dot{x}(\tau) = \dfrac{\mathrm{d}x(\tau)}{\mathrm{d}\tau} = v_x(\tau), \\[2mm]
\dot{y}(\tau) = \dfrac{\mathrm{d}y(\tau)}{\mathrm{d}\tau} = v_y(\tau), \\[2mm]
\dot{v}_x(\tau) = \dfrac{\mathrm{d}v_x(\tau)}{\mathrm{d}\tau} = g\tan\alpha(\tau)\cos\psi(\tau) \\[2mm]
\qquad\qquad\qquad - \operatorname{sign}(v_x(\tau))\dfrac{C_d}{m_u}v_x(\tau)^2, \\[2mm]
\dot{v}_y(\tau) = \dfrac{\mathrm{d}v_y(\tau)}{\mathrm{d}\tau} = g\tan\alpha(\tau)\sin\psi(\tau) \\[2mm]
\qquad\qquad\qquad - \operatorname{sign}(v_y(\tau))\dfrac{C_d}{m_u}v_y(\tau)^2,
\end{cases}
\tag{8}
$$

where v_x and v_y represent the velocity on the x axis and y axis, respectively.

Observing the dynamic model (8), both the position and velocity of a UAV can be optimized by designing the attack angle $\alpha(\tau)$ and the heading angle $\psi(\tau)$.

B. Channel Model

There exist three main types of aerial link models between the UAV and the GN in the existing literature. In [32], a fading channel for the UAV-GN link is considered, in which both types of fading effects are considered. Probabilistic line-of-sight (LoS) channel models are used in [24], [29], and [33], where the probability of the unobstructed direct link is determined by the environment, elevation angle, and communication distance. In [4], [20], [21], [34]–[37], the widely adopted free-space pathloss link is introduced in the channel model between the UAV and the GN, which is dominated by the LoS link, and this model is also adopted in this paper.

We suppose that there are no obstructions in the direct paths between the UAV and the GNs. Furthermore, the high-speed rotation of the UAV rotor blades may cause changes in the surrounding physical field (such as air flow, pressure, sound or electromagnetic field) [38]. The modeling of such effects is particularly complicated and is not the focus of this paper, thus this paper will not consider such effects. Moreover, it is supposed that the Doppler effect induced by the UAV motion is fully compensated. Hence, the aerial channel between the UAV and the GN is predominantly characterized by LoS links with a given path loss exponent and random phases, as given by[2]

$$
h_m(\tau) = \sqrt{\beta_0 d_m^{-\iota}(\tau)}e^{j\phi_m(\tau)},
$$

where $d_m(\tau)$ represents the Euclidean distance between the UAV and the mth GN, which is defined as

$$
d_m(\tau) = \sqrt{(x(\tau) - x_m)^2 + (y(\tau) - y_m)^2 + H^2}.
$$

The uploaded data ν is modeled as a circularly symmetric complex Gaussian random variable, and $\nu \sim \mathcal{CN}(0, 1)$. Thus, the signal transmitted by the mth GN is $\sqrt{P_m(\tau)}e^{j\varphi_m(\tau)}\nu$, where $P_m(\tau) \geq 0$ is the mth GN transmit power. Besides,

[2]It is assumed that the channel knowledge is available at the UAV and GNs through channel estimation and tracking using pilot symbols or channel training sequence [39].

suppose that there is a limit on the average transmit power of the mth GN, which is denoted as P_m^{ave}. Therefore, the power constraint is defined by

$$
\int_0^T P_m(\tau)\mathrm{d}\tau \leq TP_m^{\mathrm{ave}}, \quad \forall m \in \mathcal{M}. \tag{9}
$$

Thus, the signal received by UAV is defined as

$$
\begin{aligned}
q(\tau) &= \sum_{m=1}^M h_m(\tau)\sqrt{P_m(\tau)}e^{j\varphi_m(\tau)}\nu + z \\
&= \sum_{m=1}^M \sqrt{P_m(\tau)\beta_0 d_m^{-\iota}(\tau)}e^{j(\phi_m(\tau)+\varphi_m(\tau))}\nu + z,
\end{aligned}
$$

where z stands for the additive white Gaussian noise and $z \sim \mathcal{CN}(0, \sigma^2)$. Moreover, the channel phase shift is assumed to be estimated online by GNs, thus setting $\varphi_m(\tau) = -\phi_m(\tau)$ achieves constructive signal superposition at the UAV receiver. The signal-to-noise ratio (SNR) of the UAV at time $\tau \in \mathcal{T}$ is

$$
\begin{aligned}
\mathrm{SNR}(\tau) &= \frac{\mathbb{E}\left\{\left|\sum\limits_{m=1}^M \sqrt{P_m(\tau)\beta_0 d_m^{-\iota}(\tau)}\nu\right|^2\right\}}{\mathbb{E}\left\{|z|^2\right\}} \\
&= \frac{\left(\sum\limits_{m=1}^M \sqrt{P_m(\tau)\beta_0 d_m^{-\iota}(\tau)}\right)^2}{\sigma^2}.
\end{aligned}
\tag{10}
$$

Then, the achievable data rate at time $\tau \in \mathcal{T}$ can be defined by

$$
R(\tau) = B\log_2(1 + \mathrm{SNR}(\tau)), \tag{11}
$$

where B represents the channel bandwidth. Here, the GNs are assumed to be able to adaptively change the transmit power according to the time-varying UAV-GN channel. Thus, the average transmit data rate is utilized as the metric for evaluating performance, given by[3]

$$
R^{\mathrm{ave}}(T) = \frac{1}{T}\int_0^T R(\tau)\mathrm{d}\tau \tag{12}
$$

$$
= \frac{1}{T}\int_0^T B\log_2\left(1 + \frac{\left(\sum_{m=1}^M \sqrt{P_m(\tau)\beta_0 d_m^{-\iota}(\tau)}\right)^2}{\sigma^2}\right)\mathrm{d}\tau.
$$

C. Problem Formulation

In the scenario we are considering, the goal of the mission is to maximize the average transmit data rate $R^{\mathrm{ave}}(T)$ by a joint design of the trajectory $(x(\tau), y(\tau))^\top$ and the GNs' transmit power $\tilde{\boldsymbol{P}}(\tau) = (P_1(\tau), P_2(\tau), \ldots, P_M(\tau))^\top$. Furthermore, the UAV dynamic constraints (8), the GNs average transmit power constraints (9) and physical constraints (velocity, attack angle and heading angle) are required to be satisfied. As mentioned, the trajectory $(x(\tau), y(\tau))^\top$ of UAV is determined by $(\alpha(\tau), \psi(\tau))^\top$ according to (8). Thus, $(\alpha(\tau), \psi(\tau), \tilde{\boldsymbol{P}}(\tau))^\top$ are chosen as decision variables.

[3]By breaking down the interval $[0, T]$ into smaller intervals corresponding to the burst periods, such as $[0, t_1]$ and $[t_2, t_3]$, where $0 < t_1 < t_2 < t_3 < T$, we can adapt the continuous transmission model given in (12) to accommodate burst transmission. Therefore, our transmission model is general in that burst transmission can be viewed as a special case of continuous transmission.

The dynamic optimization problem is formulated as below, which is referred to as problem P1:

P1 :

$$\max_{\alpha(\tau),\psi(\tau),\tilde{\boldsymbol{P}}(\tau)} R^{\text{ave}}(T)$$

$$\text{s.t.} \quad (8), (9),$$

$$P_m(\tau) \geq 0, \ \forall m \in \mathcal{M}, \ \forall \tau \in \mathcal{T}, \quad (13a)$$

$$|\alpha(\tau)| \leq \alpha_{max}, \ |\psi(\tau)| \leq \psi_{max}, \ \forall \tau \in \mathcal{T}, \quad (13b)$$

$$\sqrt{v_x(\tau)^2 + v_y(\tau)^2} \leq V_{\max}, \ \forall \tau \in \mathcal{T}, \quad (13c)$$

$$x(0) = x_0, \ y(0) = y_0, \ v_x(0) = v_x^0,$$
$$v_y(0) = v_y^0, \quad (13d)$$

$$x(T) = x_F, \ y(T) = y_F. \quad (13e)$$

In problem P1, (13a) is the transmit power constraint, while (13b) and (13c) are the physical constraints of UAV. In real world applications, (13b) is required to limit the maneuverability of the UAV, where α_{max} and ψ_{max} are the maximum budget of $\alpha(\tau)$ and $\psi(\tau)$, respectively. (13c) is the velocity constraint, where V_{max} is the maximum allowable velocity. (13d) and (13e) are the given start point and end point constraints, respectively.

REMARK 1: P1 is essentially a dynamic optimization problem as the dynamic constraints are imposed. In addition, the physical constraints (13b) and (13c) are infinite-dimensional in nature, which are difficult to handle. Therefore, it is not an easy task to solve P1.

III. PROPOSED SOLUTION METHOD

In order to address these challenges from the dynamic and physical constraints, an efficient algorithm[4] is developed in this section. In particular, the control parametrization scheme will be utilized to handle the dynamic constraints while an exact penalty function method will be leveraged to tackle the physical constraints.

A. Control Parametrization

For notational brevity, we define the state vector

$$\boldsymbol{s}(\tau) = [x(\tau), y(\tau), v_x(\tau), v_y(\tau)]^\top, \quad (14)$$

and the control vector

$$\boldsymbol{c}(\tau) = \left[\alpha(\tau), \psi(\tau), \tilde{\boldsymbol{P}}(\tau)\right]^\top, \quad (15)$$

respectively.

Then, we equally discretize the time horizon $[0, T]$ into N intervals $[\tau_{n-1}, \tau_n)$, $\forall n \in \mathcal{N} \triangleq \{1, 2, \ldots, N\}$. Letting $\xi = T/N$, we have

$$\left\{\tau_0 = 0, \tau_1 = \xi, \tau_2 = 2\xi, ..., \tau_{N-1} = (N-1)\xi, \tau_N = T\right\}.$$

[4]The algorithms developed are applicable not only to UAV data collection scenarios involving multiple GNs, but also to UAVs with different dynamic models. This is because the proposed algorithm can transform the infinite-dimensional dynamic programming problem into a finite-dimensional static nonlinear problem, and is therefore unaffected by differences in dynamic models.
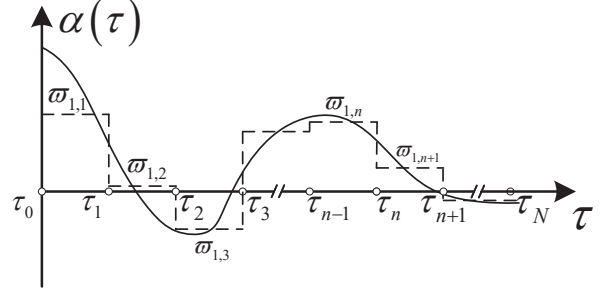

Fig. 3: An illustration of control parametrization.

Next, as illustrated in Fig. 3, the continuous variable $\alpha(\tau)$ is parameterized by a piecewise constant function $\varpi_{1,n}, n = 1, 2, \ldots, N$, i.e., $\alpha(\tau) \approx \sum_{n=1}^{N} \varpi_{1,n} \Xi_{[\tau_{n-1}, \tau_n)}(\tau)$. Thus, the control variables $c_i(\tau)$, $\forall i \in \mathcal{I} \triangleq \{1, 2, \ldots, M+2\}$ are approximated as follow:

$$c_i(\tau) \approx \sum_{n=1}^{N} \varpi_{i,n} \Xi_{[\tau_{n-1}, \tau_n)}(\tau), \quad (16)$$

where $\Xi_{[\tau_{n-1}, \tau_n)}(\tau) : \mathbb{R} \to \mathbb{R}$ denotes the characteristic function expressed as

$$\Xi_{[\tau_{n-1}, \tau_n)}(\tau) = \begin{cases} 1, & \tau \in [\tau_{n-1}, \tau_n), \\ 0, & \tau \notin [\tau_{n-1}, \tau_n), \end{cases}$$

and $\varpi_{i,n}$ represents the approximate value of $c_i(\tau)$ on the subinterval $[\tau_{n-1}, \tau_n)$. Now, for each $i \in \mathcal{I}$, define $\boldsymbol{\varpi}_i = [\varpi_{i,1}, \varpi_{i,2}, \ldots, \varpi_{i,N}]^\top$. On this basis, define the following vector:

$$\boldsymbol{\varpi} = \left[\boldsymbol{\varpi}_1^\top, \boldsymbol{\varpi}_2^\top, \ldots, \boldsymbol{\varpi}_{M+2}^\top\right]^\top. \quad (17)$$

In fact, the infinite-dimensional control vector $\boldsymbol{c}(\tau)$, $\tau \in \mathcal{T}$, is parameterized by $\boldsymbol{\varpi}$.

Hence, the dynamic model (8) on $[\tau_{n-1}, \tau_n)$ is rewritten as:

$$\begin{cases} \dot{x}(\tau) = v_x(\tau), \\ \dot{y}(\tau) = v_y(\tau), \\ \dot{v}_x(\tau) = g \tan \varpi_{1,n} \cos \varpi_{2,n} - \text{sign}(v_x(\tau)) \dfrac{C_d}{m_u} v_x(\tau)^2, \\ \dot{v}_y(\tau) = g \tan \varpi_{1,n} \sin \varpi_{2,n} - \text{sign}(v_y(\tau)) \dfrac{C_d}{m_u} v_y(\tau)^2. \end{cases} \quad (18)$$

We represent the above system in the following form:

$$\dot{\boldsymbol{s}}(\tau) = \boldsymbol{g}(\tau, \boldsymbol{s}(\tau \,|\, \boldsymbol{\varpi}), \boldsymbol{\varpi}). \quad (19)$$

In view of (13a) and (13b), the control value in (17) must satisfy

$$0 \leq \varpi_{i,n}, \ i = 3, \ldots, M+2, \quad (20)$$

$$-\alpha_{max} \leq \varpi_{1,n} \leq \alpha_{max}, \ -\psi_{max} \leq \varpi_{2,n} \leq \psi_{max}. \quad (21)$$

Substituting (16) into (12), it is not difficult to get that

$$R^{\text{ave}}(T) = \frac{1}{T} \sum_{n=1}^{N} \int_{\tau_{n-1}}^{\tau_n} R_2(\tau) \mathrm{d}\tau, \qquad (22)$$

where

$$R_2(\tau) = B\log_2\left(1 + \frac{\left(\sum_{i=3}^{M+2} \sqrt{\varpi_{i,n}\beta_0 d_i^{-\iota}(\tau)}\right)^2}{\sigma^2}\right).$$

REMARK 2: Different from existing works (for example, [23]), only the decision variables are discretized. By solving (8) with the parametrized function (16) piecewise, as in (18), the obtained trajectory $\{x(\tau), y(\tau)\}$, $\forall \tau \in \mathcal{T}$ is smooth. Furthermore, if $\boldsymbol{c}(\tau)$ is approximated by piece-wise linear (first-order polynomial), piece-wise quadratic (second-order polynomial) or spline functions, a continuous or a smooth parametrization of $\boldsymbol{c}(\tau)$ can be obtained.

B. An Exact Penalty Function Method

In order to handle the continuous inequality constraint (13c) and the terminal constraints (9), (13e), we introduce an exact penalty function method [40].

First, we define

$$\mathcal{F}_\epsilon = \Big\{ (\boldsymbol{\varpi}, \epsilon) \in \Upsilon \times [0, \epsilon_{\max}] :$$
$$\sqrt{v_x(\tau)^2 + v_y(\tau)^2} - V_{\max} \leq \epsilon^\gamma E_1, \forall \tau \in \mathcal{T} \Big\}. (23)$$

In particular, when $\epsilon = 0$, let

$$\mathcal{F}_0 = \Big\{ \boldsymbol{\varpi} \in \Upsilon : \sqrt{v_x(\tau)^2 + v_y(\tau)^2} - V_{\max} \leq 0, \forall \tau \in \mathcal{T} \Big\}. \tag{24}$$

Similarly, we define

$$\mathcal{G}_\epsilon = \Big\{ (\boldsymbol{\varpi}, \epsilon) \in \mathcal{F}_\epsilon : x(T) - x_F = 0, y(T) - y_F = 0,$$
$$\frac{1}{T} \sum_{n=1}^{N} \varpi_{i,n}\xi - P_{i-2}^{\text{ave}} \leq \epsilon^\gamma E_{i-1}, \forall \tau \in \mathcal{T}, i = 3, \dots, M+2 \Big\},$$
$$\tag{25}$$

and

$$\mathcal{G}_0 = \Big\{ \boldsymbol{\varpi} \in \mathcal{F}_0 : x(T) - x_F = 0, y(T) - y_F = 0,$$
$$\frac{1}{T} \sum_{n=1}^{N} \varpi_{i,n}\xi - P_{i-2}^{\text{ave}} \leq 0, \forall \tau \in \mathcal{T}, i = 3, \dots, M+2 \Big\}, \tag{26}$$

where $E_i \in (0,1)$, $i = 1, 2, \dots, M+1$, are given constants, γ is fixed number satisfying $\gamma > 0$, and $\epsilon_{\max}$ is a given constant.

Then, an exact penalty function introduced in [40] is applied. We construct a new objective function (27), which is shown at the top of this page. Specifically, the reformulated objective function consists of two main parts, the original objective function in (22) and the integral form of the exact penalty function. In (27), ϵ is the introduced decision variable, we impose the bound constraint on $\epsilon \in [0, \epsilon_{\max}]$. Moreover, $O(\boldsymbol{s}(\tau), \boldsymbol{\varpi})$ in (27) is

$$O(\boldsymbol{s}(\tau \,|\, \boldsymbol{\varpi}), \boldsymbol{\varpi}) = -R^{\text{ave}}(T).$$

Furthermore, $\aleph(\boldsymbol{s}(\tau), \boldsymbol{\varpi}, \epsilon)$ and $\aleph_1$ in (27) are respectively defined by

$$\aleph(\boldsymbol{s}(\tau), \boldsymbol{\varpi}, \epsilon)$$
$$= \int_0^T \left[\max\left\{0, \sqrt{v_x(\tau)^2 + v_y(\tau)^2} - V_{\max} - \epsilon^\gamma E_1\right\}\right]^2 \mathrm{d}\tau, \tag{28}$$

and

$$\aleph_1 = (x(T) - x_F)^2 + (y(T) - y_F)^2$$
$$+ \sum_{i=3}^{M+2} \left[\max\left\{0, \frac{1}{T}\sum_{n=1}^{N}\varpi_{i,n}\xi - P_{i-2}^{\text{ave}} - \epsilon^\gamma E_{i-1}\right\}\right]^2. \tag{29}$$

Moreover, in (27), $\vartheta > 0$ is the penalty parameter, and δ, β are fixed numbers satisfying $\delta > 0$, $\beta > 2$.

REMARK 3: In the optimization process, if the penalty parameter ϑ is increased, ϵ^β needs to be reduced to minimize O_ϑ. This means that ϵ must decrease since β is fixed. As ϵ decreases, $\epsilon^{-\delta}$ will increase. Thus, the values of $\aleph(\boldsymbol{s}(\tau), \boldsymbol{\varpi}, \epsilon)$ and $\aleph_1$ must reduce, giving rise to the satisfaction of the continuous inequality constraint (13c), the terminal constraint (13e), and the power constraint (9).

C. Proposed Algorithm

Based on the discussion above, P1 can be converted into the following problem which is referred to as $(\text{P1})_\vartheta$, given by

$$(\mathbf{P1})_\vartheta : \quad \min_{\boldsymbol{\varpi}, \epsilon} \quad O_\vartheta(\boldsymbol{s}(\tau \,|\, \boldsymbol{\varpi}), \boldsymbol{\varpi}, \epsilon)$$
$$s.t. \quad 0 \leq \epsilon \leq \epsilon_{max}, \tag{30}$$
$$(13d),\ (18),\ (20),\ (21).$$

By (27), (28) and (29), we can organize the objective function into the following form

$$O_\vartheta(\boldsymbol{s}(\tau \,|\, \boldsymbol{\varpi}), \boldsymbol{\varpi}, \epsilon)$$
$$= \tilde{\Theta}_0(\boldsymbol{s}(T \,|\, \boldsymbol{\varpi}), \boldsymbol{\varpi}, \epsilon) + \int_0^T \tilde{\Psi}_0(\tau, \boldsymbol{s}(\tau \,|\, \boldsymbol{\varpi}), \boldsymbol{\varpi}, \epsilon)\,\mathrm{d}\tau, \tag{31}$$

where

$$\tilde{\Theta}_0(\boldsymbol{s}(T \,|\, \boldsymbol{\varpi}), \boldsymbol{\varpi}, \epsilon)$$
$$= -R^{\text{ave}}(T) + \vartheta\epsilon^\beta + \epsilon^{-\delta}\Big\{(x(T) - x_F)^2 + (y(T) - y_F)^2$$
$$+ \sum_{i=3}^{M+2} \left[\max\left\{0, \frac{1}{T}\sum_{n=1}^{N}\varpi_{i,n}\xi - P_{i-2}^{\text{ave}} - \epsilon^\gamma E_{i-1}\right\}\right]^2\Big\}, \tag{32}$$

and

$$\tilde{\Psi}_0(\tau, \boldsymbol{s}(\tau \,|\, \boldsymbol{\varpi}), \boldsymbol{\varpi}, \epsilon)$$
$$= \epsilon^{-\delta}\left[\max\left\{0, \sqrt{v_x(\tau)^2 + v_y(\tau)^2} - V_{\max} - \epsilon^\gamma E_1\right\}\right]^2. \tag{33}$$

Here, as long as we successfully compute the gradients of $O_\vartheta(\boldsymbol{s}(\tau \,|\, \boldsymbol{\varpi}), \boldsymbol{\varpi}, \epsilon)$ with respect to $\boldsymbol{\varpi}$ and ϵ, the solution of problem $(\text{P1})_\vartheta$ will be obtained through the standard optimization method such as SQP. This is because (20), (21), and (30) are box constraints on the decision variables. In addition, (13d) is the initial condition of dynamic constraints

$$O_\vartheta\left(s(\tau\,|\,\varpi),\varpi,\epsilon\right) = \begin{cases} O\left(s(\tau\,|\,\varpi),\varpi\right) & \epsilon = 0, \varpi \in \mathcal{G}_0, \\ O\left(s(\tau\,|\,\varpi),\varpi\right) + \epsilon^{-\delta}\left(\aleph\left(s(\tau),\varpi,\epsilon\right)+\aleph_1\right)+\vartheta\epsilon^\beta & \epsilon > 0, \\ \infty & \text{otherwise.} \end{cases} \tag{27}$$

(18) and it can be used to solve for $s(\tau)$ with the current decision variables ϖ and ϵ at each iteration step. Thus, the derivation of the gradient formulas is a crucial process for implementing the proposed method and it will be given in the next subsection.

According to [40], [41], a locally optimal solution of problem P1 can be computed via solving a sequence of problems $(P1)_\vartheta$ by adjusting ϵ and ϑ, which are summarized in Algorithm 1. Moreover, the details for solving problem $(P1)_\vartheta$ are presented in Algorithm 2. In the initial optimization phase, to mitigate the penalty for constraint violations, the optimizer can set a larger value of ϵ to reduce the penalty weight and loosen the constraints. As the number of constraint violations gradually decreases, the optimizer can progressively decrease the value of ϵ to increase the penalty weight and tighten the constraints, further inhibiting the occurrence of violations. It is important to note that decreasing ϵ reduces penalty $\vartheta\epsilon^\beta$, thereby promoting the reduction of the objective function. Based on section 9.3.2 of [41], if the iteration $k \to \infty$, then $\epsilon^{(k)} \to 0$, $(\varpi_\vartheta^{(k),*}, \epsilon^{(k),*}) \to (\varpi_\vartheta^*, \epsilon^*)$ is a local minimizer of problem P1. Thus, Algorithm 1 is convergent.

The computational complexities of [23], P1 and P1 with 6-DoF model are listed in Table II. Despite the method proposed in [23] having a lower complexity than our proposed method, it fails to consider the dynamics of UAV, obtaining a set of discrete trajectory points that are difficult for the UAV to actually follow. It is noteworthy that the continuous trajectory obtained for problem P1, which does not employ a 6-DoF model that can more accurately describe the UAV's motion state, cannot be precisely followed by the UAV. Nevertheless, the complexity of solving problem P1 is lower than that of solving problem P1 with the 6-DoF model. Therefore, the proposed method successfully achieves a good trade-off between performance and complexity when solving problem P1.

REMARK 4: The convergence of $\varpi_\vartheta^{(k)}$ to a locally optimal solution $c^*(\tau)$ with Algorithm 2 can be guaranteed by Theorems 9.3.2, 9.3.3, and 9.3.4 of [41].

TABLE II: Computational Complexity

[23]	P1	P1 with 6-DoF
$\mathbb{O}\left((MN+2N)^{3.5}\right)$	$\mathbb{O}\left((2MN+4N)^{3.5}\right)$	$\mathbb{O}\left((2MN+8N)^{3.5}\right)$

D. Gradient Formulas

In this subsection, we give the gradient formulas of $O_\vartheta(s(\tau\,|\,\varpi),\varpi,\epsilon)$ with respect to ϖ and ϵ which are essential for solving problem $(P1)_\vartheta$.

Theorem 1

Algorithm 1 Solving P1

Input: ϖ_0.
Output: ϖ^*.
Initialization: $k = 0$, $\vartheta^{(0)} = 10$, $\epsilon^{(0)} = 0.1$, $\vartheta_{max} = 10^8$, $\epsilon_{min} = 10^{-9}$, $\beta > 2$, $\varpi_\vartheta^{(0)} = \varpi_0$.
1: Solve problem $(P1)_\vartheta$ with $(\varpi_\vartheta^{(k)}, \epsilon^{(k)})$ as initial point, and denote the minimum obtained as $(\varpi_\vartheta^{(k),*}, \epsilon^{(k),*})$. Calculate $s^{(k),*}$ according to (18).
2: **While** $\epsilon^{(k),*} > \epsilon_{min}$, $\vartheta^{(k)} < \vartheta_{max}$ **do**
3:    Set $\vartheta^{(k+1)} = 10\vartheta^{(k)}$, $\varpi_\vartheta^{(k+1)} = \varpi_\vartheta^{(k),*}$, $\epsilon^{(k+1)} = \epsilon^{(k),*}$ $k = k + 1$, then back to Step 1.
4: **End while**
5: Set $\epsilon^{(k),*} = \epsilon_{min}$.
6: **If** $s^{(k),*}$ is feasible **do**
7:    Exit.
8: **Else**
9:    Adjust δ, β, and γ. Set $\vartheta^{(k+1)} = 10\vartheta^{(k)}$, $\epsilon^{(k+1)} = 0.1\epsilon^{(k)}$, $k = k + 1$, then back to Step 1.
10: **End if**
11: Output $\varpi^* = \varpi_\vartheta^{(k),*}$.

Algorithm 2 Solving $(P1)_\vartheta$

Input: $\varpi_\vartheta^{(k)}$ and $\epsilon^{(k)}$.
Output: $\varpi_\vartheta^{(k+1)}$ and $\epsilon^{(k+1)}$.
1: Calculate the control vector $c^{(k)}(\tau)$ with $\varpi_\vartheta^{(k)}$ according to (16).
2: Calculate the state vector $s^{(k)}(\tau)$ from the differential equations (8).
3: Derive the gradients of $O_\vartheta(s(\tau\,|\,\varpi),\varpi,\epsilon)$ with respect to $\varpi_\vartheta^{(k)}$ and $\epsilon^{(k)}$.
4: The values and gradients of the objective function as well as the box constraints are input to the nonlinear program solver.
5: Output $\varpi_\vartheta^{(k+1)}$ and $\epsilon^{(k+1)}$.

(i) The gradient of $O_\vartheta(s(\tau\,|\,\varpi),\varpi,\epsilon)$ with respect to each component of ϖ is

$$\frac{\partial O_\vartheta(s(\tau\,|\,\varpi),\varpi,\epsilon)}{\partial \varpi_i} = \Lambda_i^\top + \lambda_1^\top v_i(T\,|\,\varpi)$$
$$+ \int_0^T \left(X_i^\top + \lambda_2^\top v_i(\tau\,|\,\varpi)\right) d\tau, \ \forall i \in \mathcal{I}, \tag{34}$$

where $v_i(\tau)$ satisfies the following differential equation,

$$\frac{dv_i(\tau)}{d\tau} = \frac{\partial g(\tau, s(\tau\,|\,\varpi),\varpi)}{\partial s}v_i(\tau) + \frac{\partial g(\tau, s(\tau\,|\,\varpi),\varpi)}{\partial \varpi_i} \tag{35}$$

This article has been accepted for publication in IEEE Transactions on Communications. This is the author's version which has not been fully edited and content may change prior to final publication. Citation information: DOI 10.1109/TCOMM.2025.3543221

8

with the initial condition $\boldsymbol{v}_i(0) = \mathbf{0}_{4 \times N}$. Here,

$$\boldsymbol{\Lambda} = \begin{bmatrix} \boldsymbol{\Lambda}_1^\top \\ \boldsymbol{\Lambda}_2^\top \\ \boldsymbol{\Lambda}_3^\top \\ \cdots \\ \boldsymbol{\Lambda}_{M+2}^\top \end{bmatrix} = \begin{bmatrix} 0 & 0 & \cdots & 0 \\ 0 & 0 & \cdots & 0 \\ \Lambda_{3,1} & \Lambda_{3,2} & \cdots & \Lambda_{3,N} \\ \cdots & & & \\ \Lambda_{M+2,1} & \Lambda_{M+2,2} & \cdots & \Lambda_{M+2,N} \end{bmatrix}, \quad (36)$$

$$\Lambda_{i,n} = \frac{2\epsilon^{-\delta}\xi}{T} \left[\max \left\{ 0, \frac{1}{T} \sum_{n=1}^N \varpi_{i,n}\xi - P_{i-2}^{\text{ave}} - \epsilon^\gamma E_{i-1} \right\} \right]$$
$$- \frac{1}{T} B \log_2 \left(1 + \frac{1}{2\sigma^2} \sqrt{\frac{\beta_0 d_i^{-\iota}(\tau)}{\varpi_{i,n}}} \right).$$

$$\mathbf{X} = \begin{bmatrix} \mathbf{X}_1^\top \\ \mathbf{X}_2^\top \\ \cdots \\ \mathbf{X}_{M+2}^\top \end{bmatrix} = \begin{bmatrix} \mathbf{0}_{1 \times N} \\ \mathbf{0}_{1 \times N} \\ \cdots \\ \mathbf{0}_{1 \times N} \end{bmatrix}, \quad (37)$$

$$\boldsymbol{\lambda}_1 = -\frac{B}{T} \begin{bmatrix} \lambda_{1,1} & \lambda_{1,2} & 0 & 0 \end{bmatrix}^\top, \quad (38)$$

$$\lambda_{1,1} = \sum_{n=1}^N \log_2 \left(1 - \frac{\sum_{i=3}^{M+2} \left(\sqrt{\varpi_{i,n}\beta_0} d_i^{-(\iota+1)} \iota(x(\tau) - x_i) \right)}{\sigma^2} \right),$$

$$\lambda_{1,2} = \sum_{n=1}^N \log_2 \left(1 - \frac{\sum_{i=3}^{M+2} \left(\sqrt{\varpi_{i,n}\beta_0} d_i^{-(\iota+1)} \iota(y(\tau) - y_i) \right)}{\sigma^2} \right).$$

$$\boldsymbol{\lambda}_2 = \lambda_2 \begin{bmatrix} 0 & 0 & v_x(\tau)^2 & v_y(\tau)^2 \end{bmatrix}^\top, \quad (39)$$

$$\lambda_2 = 2\epsilon^{-\delta} \frac{\max \left\{ 0, \sqrt{v_x(\tau)^2 + v_y(\tau)^2} - V_{\max} - \epsilon^\gamma E_1 \right\}}{\sqrt{v_x(\tau)^2 + v_y(\tau)^2}}.$$

$$\frac{\partial \boldsymbol{g}}{\partial \boldsymbol{s}} = \begin{bmatrix} 0 & 0 & 1 & 0 \\ 0 & 0 & 0 & 1 \\ 0 & 0 & -\frac{2C_d}{m_u}\text{sign}(v_x)v_x & 0 \\ 0 & 0 & 0 & -\frac{2C_d}{m_u}\text{sign}(v_y)v_y \end{bmatrix}. \quad (40)$$

Since $\boldsymbol{g}(\tau, \boldsymbol{s}(\tau | \boldsymbol{\varpi}), \boldsymbol{\varpi})$ is independent of $\boldsymbol{\varpi}_i$, $i = 3, 4, \cdots, M+2$, then has $\frac{\partial \boldsymbol{g}}{\partial \boldsymbol{\varpi}_i} = \mathbf{0}_{4 \times N}$, $i = 3, 4, \cdots, M+2$, and

$$\frac{\partial \boldsymbol{g}}{\partial \boldsymbol{\varpi}_1} = g \begin{bmatrix} 0 & 0 & \cdots & 0 \\ 0 & 0 & \cdots & 0 \\ \frac{\cos \varpi_{2,1}}{(\cos \varpi_{1,1})^2} & \frac{\cos \varpi_{2,2}}{(\cos \varpi_{1,2})^2} & \cdots & \frac{\cos \varpi_{2,N}}{(\cos \varpi_{1,N})^2} \\ \frac{\sin \varpi_{2,1}}{(\cos \varpi_{1,1})^2} & \frac{\sin \varpi_{2,2}}{(\cos \varpi_{1,2})^2} & \cdots & \frac{\sin \varpi_{2,N}}{(\cos \varpi_{1,N})^2} \end{bmatrix}, \quad (41)$$

$$\frac{\partial \boldsymbol{g}}{\partial \boldsymbol{\varpi}_2} = g \begin{bmatrix} 0 & \cdots & 0 \\ 0 & \cdots & 0 \\ -\tan \varpi_{1,1}\sin \varpi_{2,1} & \cdots & -\tan \varpi_{1,N}\sin \varpi_{2,N} \\ \tan \varpi_{1,1}\cos \varpi_{2,1} & \cdots & \tan \varpi_{1,N}\cos \varpi_{2,N} \end{bmatrix}. \quad (42)$$

(ii) The gradient of $O_\vartheta(\boldsymbol{s}(\tau), \boldsymbol{\varpi}, \epsilon)$ with respect to ϵ is given by

$$\frac{\partial O_\vartheta(\boldsymbol{s}(\tau), \boldsymbol{\varpi}, \epsilon)}{\partial \epsilon}$$
$$= (-\delta)\epsilon^{-\delta-1}\tilde{g}_1 + (-2\gamma)\epsilon^{\gamma-\delta-1}\tilde{g}_2 + \vartheta\beta\epsilon^{\beta-1}, \quad (43)$$

where

$$\tilde{g}_1 = (x(T) - x_F)^2 + (y(T) - y_F)^2$$
$$+ \sum_{i=3}^{M+2} \left[\max \left\{ 0, \frac{1}{T} \sum_{n=1}^N \varpi_{i,n}\xi - P_{i-2}^{\text{ave}} - \epsilon^\gamma E_{i-1} \right\} \right]^2$$
$$+ \int_0^T \left[\max \left\{ 0, \sqrt{v_x(\tau)^2 + v_y(\tau)^2} - V_{\max} - \epsilon^\gamma E_1 \right\} \right]^2 d\tau,$$

$$\tilde{g}_2 = \sum_{i=3}^{M+2} E_{i-1} \max \left\{ 0, \frac{1}{T} \sum_{n=1}^N \varpi_{i,n}\xi - P_{i-2}^{\text{ave}} - \epsilon^\gamma E_{i-1} \right\}$$
$$+ \int_0^T E_1 \max \left\{ 0, \sqrt{v_x(\tau)^2 + v_y(\tau)^2} - V_{\max} - \epsilon^\gamma E_1 \right\} d\tau.$$

Proof: See Appendix A.

IV. NUMERICAL RESULTS

TABLE III: Parameters for Simulations

m_u	3 kg	B	1 MHz
g	9.8 m/s²	V_{max}	40 m/s
H	50 m	C_d	0.11 N/(m/s)²
N	40	α_{max}	1.57 rad
ψ_{max}	1 rad	β_0	-30 dB
ι	2.8	σ^2	-60 dBm

In this section, the effectiveness of our proposed algorithm is demonstrated with numerical examples. To show the superiority of our proposed scheme, we consider the benchmark scheme [23] without a dynamic model (8) for comparison[5]. Unless stated otherwise, the problem parameters are listed in Table III.

A. Example 1: One-GN

In this example, the scenario with a single GN is considered. The UAV's start and end points, GN's location are set to [0, 50m], [200m, 50m] and [100m, 200m], respectively.

In Fig. 5 and Fig. 6, we plot the planned and actual trajectories obtained by the proposed method and [23], and T is set as 40 seconds. The actual trajectories are obtained by tracking the planned trajectories using a proportional-integral-derivative (PID) controller with the 6-DoF UAV model [29], which not only considers the translational motion but also considers the rotational motion of the UAV[6], as illustrated in Fig. 4. As shown in Fig. 5 and Fig. 6, the planned trajectories

---

[5]There are two reasons why [23] serves as the benchmark. On the one hand, [23] and this work share similarities in channel modeling and problem formulation, except for the UAV dynamic model (8). On the other hand, the algorithm proposed by [23] adopts methods commonly used in existing works, such as time discretization and the convex optimization technique, to construct piecewise trajectory design schemes, thus it can be regarded as a representative of existing research works. Therefore, [23] is used as a benchmark for a better understanding of the performance changes caused by ignoring the UAV dynamic model under existing research methods.

[6]The PID controller designed by the 6-DoF model can calculate the control instructions of UAV in actual flight according to the motion parameter information and the expected trajectory of the UAV. These control instructions can then be converted by simulated actuator (such as motor and steering gear) into the actual actions of the UAV (such as lifting, pitching and yawing), to simulate the actual flight of the UAV.

Planned Trajectory → Tracking Controller → Control Quantity → UAV Motor Speed Calculation → Motor Speed → UAV 6-DoF Model → Actual Trajectory
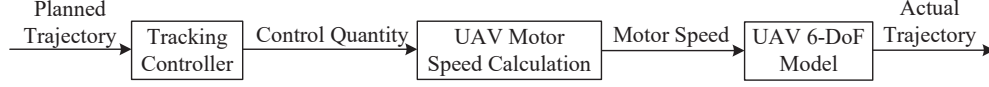
Fig. 4: The design framework of PID controller.

of the two schemes attempt to approach the GN to improve the system throughput during the flight from the start point to the end point. However, compared with the proposed scheme, the actual trajectory of [23] fails to reach the end point. This is because the dynamics of the UAV mentioned above are ignored, and hence the planned trajectory cannot be fully tracked by the UAV controller to finish the main task.

The average throughput versus T for different trajectories is plotted in Fig. 7. As illustrated in Fig. 7, the average throughput gradually increases as T becomes larger. In addition, the communication performance of [23] is better than that of the proposed scheme with the planned trajectory. This is due to the fact that the feasible solution space of [23] is broader, as it does not take into account the UAV motion model. In other words, the benchmark scheme is no longer limited by the motion characteristics of the UAV, allowing it to explore more freely within a wider solution space. Thus, this increases the likelihood that the benchmark scheme will find a planned trajectory with superior communication performance. Furthermore, the average throughput of the planned trajectories is higher than that of the actual trajectories under both of the schemes. This further verifies that performance degradation may occur if the dynamics are ignored or simplified. However, the performance loss of the proposed method is much less than that of [23], demonstrating the superiority of the proposed method.
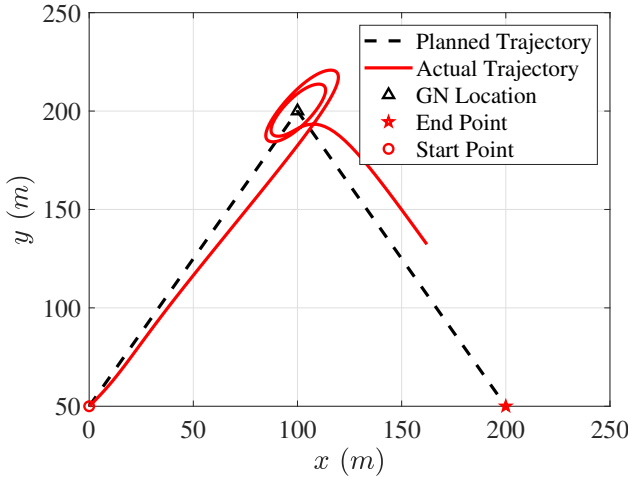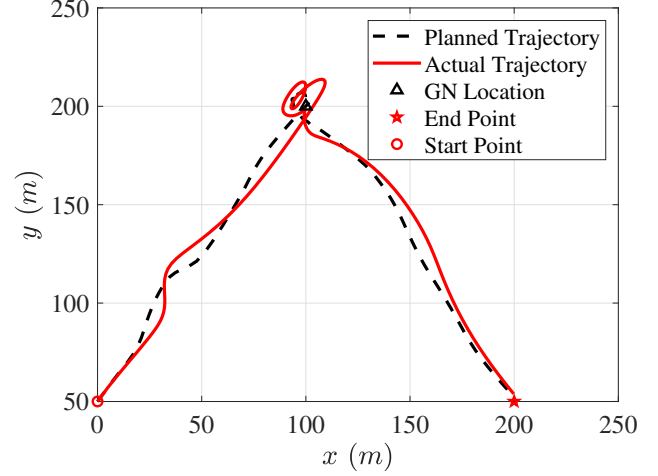
Fig. 6: Example 1: The planned and actual trajectories of the proposed method.

Fig. 7: Example 1: Average data throughput comparison in the one-GN case.

Fig. 5: Example 1: The planned and actual trajectories of [23].

B. Example 2: Multi-GN

In this example, multiple GNs are considered. Here, we consider 10 GNs, and they are located at $\boldsymbol{o}_1 = [20\text{m}, 10\text{m}]$, $\boldsymbol{o}_2 = [30\text{m}, 28\text{m}]$, $\boldsymbol{o}_3 = [46\text{m}, 0]$, $\boldsymbol{o}_4 = [56\text{m}, 24\text{m}]$, $\boldsymbol{o}_5 = [94\text{m}, 168\text{m}]$, $\boldsymbol{o}_6 = [100\text{m}, 200\text{m}]$, $\boldsymbol{o}_7 = [112\text{m}, 176\text{m}]$, $\boldsymbol{o}_8 = [162\text{m}, 0]$, $\boldsymbol{o}_9 = [178\text{m}, 40\text{m}]$, and $\boldsymbol{o}_{10} = [200\text{m}, 6\text{m}]$. The start and end points of UAV are set to $[0, 0]$ and $[200\text{m}, 200\text{m}]$, respectively.

The planned and actual trajectories generated by [23] and the proposed method with $T = 40\ s$ are plotted in Fig. 8 and Fig. 9, respectively. The communication performance versus T for the planned and actual trajectories is plotted in Fig. 10. As illustrated in Fig. 8 and Fig. 9, the planned trajectories successively visit the dense areas of GNs to establish a com-

This article has been accepted for publication in IEEE Transactions on Communications. This is the author's version which has not been fully edited and content may change prior to final publication. Citation information: DOI 10.1109/TCOMM.2025.3543221

10

munication link between the UAV and each GN for improving the average throughput. Similar to the one-GN case, the actual trajectory of [23] fails to arrive at the end point, while the actual trajectory of the proposed method succeeds in doing so. This is because the dynamics of the UAV are not considered in [23]. Moreover, as shown in Fig. 10, the average throughput of [23] is greater than that of the proposed method with the planned trajectory, while the average throughput of proposed method outperforms that of [23] with the actual trajectory. Thus, a larger performance loss in [23] is resulted compared with the proposed method in the multi-GN scenario.
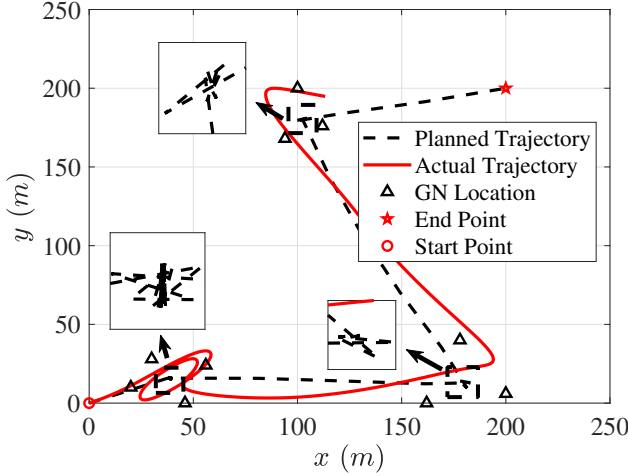

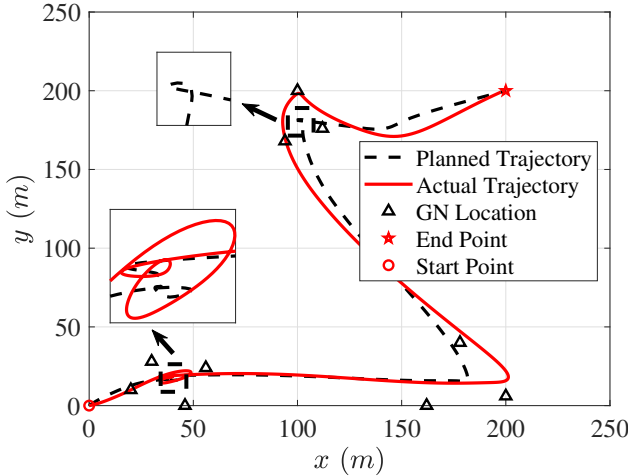Fig. 8: Example 2: The planned and actual trajectories of [23].

Fig. 9: Example 2: The planned and actual trajectories of the proposed method.

V. CONCLUSION

A control-based method has been proposed in this paper for the joint design of transmit power and trajectory in UAV-enabled data collection. Different from most previous works, dynamic constraints of the UAV have been considered and
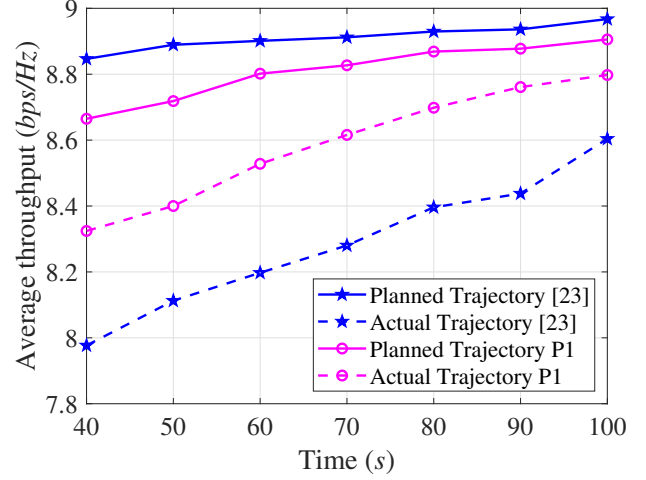

Fig. 10: Example 2: Average data throughput comparison in the multi-GN case.

smooth flying trajectories have been obtained. These trajectories have been shown to be trackable by the controller in real world applications. In contrast, piece-wise line segments were obtained with the existing works, which resulted in sharp performance degradation due to the ignoring of dynamic constraints. The advantages of the proposed method have also been demonstrated by the numerical results.

APPENDIX A
PROOF OF THEOREM 1

In fact, according to the chain rule, it is not difficult to see that the gradient of $O_\vartheta(s(\tau\,|\varpi), \varpi, \epsilon)$ with respect to each component of ϖ is

$$
\begin{aligned}
\frac{\partial O_\vartheta(s(\tau\,|\varpi), \varpi, \epsilon)}{\partial \varpi_i} &= \frac{\partial \tilde{\Theta}_0\left(s\left(T\,|\varpi\right), \varpi, \epsilon\right)}{\partial \varpi_i} \\
&+ \frac{\partial \tilde{\Theta}_0\left(s\left(T\,|\varpi\right), \varpi, \epsilon\right)}{\partial s}\frac{\partial s\left(T\,|\varpi\right)}{\partial \varpi_i} \\
&+ \int_0^T \left[\frac{\partial \tilde{\Psi}_0\left(s\left(\tau\,|\varpi\right), \varpi, \epsilon\right)}{\partial \varpi_i}+\right. \\
&\left. \frac{\partial \tilde{\Psi}_0\left(s\left(\tau\,|\varpi\right), \varpi, \epsilon\right)}{\partial s}\frac{\partial s(\tau)}{\partial \varpi_i}\right]\mathrm{d}\tau.
\end{aligned} \quad (44)
$$

Since there exists an implicit relationship between the state vector $s\left(\tau\,|\varpi\right)$ and the control vector ϖ_i, thus $\frac{\partial s(\tau|\varpi)}{\partial \varpi_i}$ needs to be further computed.

First, for any $\tau \in \mathcal{T}$, we can write $s\left(\tau\,|\varpi\right)$ as

$$
s(\tau\,|\varpi) = x_0\left(\varpi\right) + \int_0^\tau g(t, s(t\,|\varpi), \varpi)\mathrm{d}t. \quad (45)
$$

Hence, the gradient of $s(\tau\,|\varpi)$ with respect to ϖ_i is written as

$$
\begin{aligned}
\frac{\partial s(\tau\,|\varpi)}{\partial \varpi_i} &= \frac{\partial s_0\left(\varpi\right)}{\partial \varpi_i} \\
&+ \int_0^\tau \left[\frac{\partial g(t, s(t\,|\varpi), \varpi)}{\partial s}\frac{\partial s(t\,|\varpi)}{\partial \varpi_i} + \frac{\partial g(t, s(t\,|\varpi), \varpi)}{\partial \varpi_i}\right]\mathrm{d}t.
\end{aligned} \quad (46)
$$

This article has been accepted for publication in IEEE Transactions on Communications. This is the author's version which has not been fully edited and content may change prior to final publication. Citation information: DOI 10.1109/TCOMM.2025.3543221

11

Next, let $\tau = 0$, from (46), we have

$$\frac{\partial s(0 \,|\, \boldsymbol{\varpi})}{\partial \boldsymbol{\varpi}_i} = \frac{\partial s_0 (\boldsymbol{\varpi})}{\partial \boldsymbol{\varpi}_i}. \tag{47}$$

Meanwhile, we take the derivative of both sides of (46) with respect to τ, then it follows that

$$\frac{\mathrm{d}}{\mathrm{d}\tau}\left(\frac{\partial s(\tau \,|\, \boldsymbol{\varpi})}{\partial \boldsymbol{\varpi}_i}\right) = \frac{\partial \boldsymbol{g}(\tau, s(\tau \,|\, \boldsymbol{\varpi}), \boldsymbol{\varpi})}{\partial s}\frac{\partial s(\tau \,|\, \boldsymbol{\varpi})}{\partial \boldsymbol{\varpi}_i}$$
$$+ \frac{\partial \boldsymbol{g}(\tau, s(\tau \,|\, \boldsymbol{\varpi}), \boldsymbol{\varpi})}{\partial \boldsymbol{\varpi}_i}. \tag{48}$$

For any $\tau \in \mathcal{T}$, we define

$$\frac{\partial s(\tau \,|\, \boldsymbol{\varpi})}{\partial \boldsymbol{\varpi}_i} = \boldsymbol{v}_i(t). \tag{49}$$

Clearly, $\boldsymbol{v}_i(\tau)$ satisfies the following system

$$\begin{cases} \boldsymbol{v}_i(0) = \dfrac{\partial s_0 (\boldsymbol{\varpi})}{\partial \boldsymbol{\varpi}_i}, \\ \dfrac{\mathrm{d}\boldsymbol{v}_i(\tau)}{\mathrm{d}\tau} = \dfrac{\partial \boldsymbol{g}(\tau, s(\tau \,|\, \boldsymbol{\varpi}), \boldsymbol{\varpi})}{\partial s}\boldsymbol{v}_i(\tau) + \dfrac{\partial \boldsymbol{g}(\tau, s(\tau \,|\, \boldsymbol{\varpi}), \boldsymbol{\varpi})}{\partial \boldsymbol{\varpi}_i}. \end{cases} \tag{50}$$

Since $s_0 (\boldsymbol{\varpi})$ is independent of $\boldsymbol{\varpi}_i$, this further obtains $\boldsymbol{v}_i(0) = \boldsymbol{0}_{4 \times N}$.

Moreover, let

$$\frac{\partial \tilde{\Theta}_0 (s (T \,|\, \boldsymbol{\varpi}), \boldsymbol{\varpi}, \epsilon)}{\partial \boldsymbol{\varpi}_i} = \boldsymbol{\Lambda}_i^{\top}, \tag{51}$$

$$\frac{\partial \tilde{\Theta}_0 (s (T \,|\, \boldsymbol{\varpi}), \boldsymbol{\varpi}, \epsilon)}{\partial s} = \boldsymbol{\lambda}_1^{\top}, \tag{52}$$

$$\frac{\partial \tilde{\Psi}_0 (s (\tau \,|\, \boldsymbol{\varpi}), \boldsymbol{\varpi}, \epsilon)}{\partial \boldsymbol{\varpi}_i} = \mathbf{X}_i^{\top}, \tag{53}$$

$$\frac{\partial \tilde{\Psi}_0 (s (\tau \,|\, \boldsymbol{\varpi}), \boldsymbol{\varpi}, \epsilon)}{\partial s} = \boldsymbol{\lambda}_2^{\top}. \tag{54}$$

Hence, substituting (49), (51), (52), (53) and (54) into (44), we can obtain (34).

Similarly, according to the chain rule, the gradient of $O_\vartheta(s(\tau \,|\, \boldsymbol{\varpi}), \boldsymbol{\varpi}, \epsilon)$ with respect to ϵ is given as follows

$$\frac{\partial O_\vartheta(s(\tau \,|\, \boldsymbol{\varpi}), \boldsymbol{\varpi}, \epsilon)}{\partial \epsilon}$$
$$= \frac{\partial \tilde{\Theta}_0 (s (T \,|\, \boldsymbol{\varpi}), \boldsymbol{\varpi}, \epsilon)}{\partial \epsilon} + \int_0^T \frac{\partial \tilde{\Psi}_0 (\tau, s (\tau \,|\, \boldsymbol{\varpi}), \boldsymbol{\varpi}, \epsilon)}{\partial \epsilon} \mathrm{d}\tau, \tag{55}$$

where

$$\frac{\partial \tilde{\Theta}_0 (s (T \,|\, \boldsymbol{\varpi}), \boldsymbol{\varpi}, \epsilon)}{\partial \epsilon}$$
$$= \vartheta \beta \epsilon^{\beta - 1} + k_1 \Bigg\{ (x(T) - x_F)^2 + (y(T) - y_F)^2$$
$$+ \sum_{i=3}^{M+2} \left[\max\left\{ 0, \frac{1}{T}\sum_{n=1}^N \varpi_{i,n}\xi - P_{i-2}^{\text{ave}} - \epsilon^\gamma E_{i-1} \right\} \right]^2 \Bigg\}$$
$$+ k_2 \Bigg\{ \sum_{i=3}^{M+2} E_{i-1} \max\left\{ 0, \frac{1}{T}\sum_{n=1}^N \varpi_{i,n}\xi - P_{i-2}^{\text{ave}} - \epsilon^\gamma E_{i-1} \right\} \Bigg\}, \tag{56}$$

and

$$\frac{\partial \tilde{\Psi}_0 (\tau, s (\tau \,|\, \boldsymbol{\varpi}), \boldsymbol{\varpi}, \epsilon)}{\partial \epsilon}$$
$$= k_1 \left[\max\left\{ 0, \sqrt{v_x(\tau)^2 + v_y(\tau)^2} - V_{\max} - \epsilon^\gamma E_1 \right\} \right]^2$$
$$+ k_2 E_1 \max\left\{ 0, \sqrt{v_x(\tau)^2 + v_y(\tau)^2} - V_{\max} - \epsilon^\gamma E_1 \right\}. \tag{57}$$

In (56) and (57), $k_1 = (-\delta)\epsilon^{-\delta-1}, k_2 = (-2\gamma)\epsilon^{\gamma-\delta-1}$. We substitute (56) and (57) into (55), and then (43) can be proved by combining the terms with the same coefficients. This completes the proof. $\qquad\square$

REFERENCES

[1] Y. Zeng, Q. Wu, and R. Zhang, "Accessing from the sky: A tutorial on UAV communications for 5G and beyond," *Proceedings of the IEEE (Invited Paper)*, vol. 107, no. 12, pp. 2327-2375, Dec. 2019.

[2] C. Zhong, J. Yao, and J. Xu, "Secure UAV communication with cooperative jamming and trajectory control," *IEEE Commun. Lett.*, vol. 23, no. 2, pp. 286-289, Feb. 2019.

[3] M. Banagar and H. Dhillon, "Performance characterization of canonical mobility models in drone cellular networks," *IEEE Trans. Wireless Commun.*, vol. 19, no. 7, pp. 4994-5009, Jul. 2020.

[4] Y. Zeng, R. Zhang, and T. Lim, "Throughput maximization for UAV-enabled mobile relaying systems," *IEEE Trans. Commun.*, vol. 64, no. 12, pp. 4983-4996, Dec. 2016.

[5] B. Zhu, E. Bedeer, H. Nguyen, R. Barton, and Z. Gao, "UAV trajectory planning for AoI-minimal data collection in UAV-aided IoT networks by transformer," *IEEE Trans. Wireless Commun.*, vol. 22, no. 2, pp. 1343-1358, Feb. 2023.

[6] X. Gao, X. Zhu, and L. Zhai, "AoI-sensitive data collection in multi-UAV-assisted wireless sensor networks," *IEEE Trans. Wireless Commun.*, vol. 22, no. 8, pp. 5185-5197, Aug. 2023.

[7] Y. Wang, M. Chen, C. Pan, K. Wang, and Y. Pan, "Joint Optimization of UAV Trajectory and Sensor Uploading Powers for UAV-Assisted Data Collection in Wireless Sensor Networks," *IEEE Internet of Things Journal.*, vol. 9, no. 13, pp. 11214-11226, July. 2022.

[8] G. Chen, X. Zhai, and C. Li, "Joint optimization of trajectory and user association via reinforcement learning for UAV-aided data collection in wireless networks," *IEEE Trans. Wireless Commun.*, vol. 22, no. 5, pp. 3128-3143, May. 2023.

[9] S. Hu, Q. Wu, and X. Wang, "Energy management and trajectory optimization for UAV-enabled legitimate monitoring systems," *IEEE Trans. Wireless Commun.*, vol. 20, no. 1, pp. 142-155, Jan. 2021.

[10] W. Lu, Y. Ding, Y. Gao, Y. Chen, Z. Ding, and A. Nallanathan, "Secure NOMA-based UAV-MEC network towards a flying eavesdropper," *IEEE Trans. Commun.*, vol. 70, no. 5, pp. 3364-3376, May 2022.

[11] C. Zhang and Y. Zeng, "Aerial-ground cost tradeoff for multi-UAV enabled data collection in wireless sensor networks," *IEEE Trans. Commun.*, vol. 68, no. 3, pp. 1937-1950, Mar. 2020.

[12] J. Chen and D. Gesbert, "Efficient local map search algorithms for the placement of flying relays," *IEEE Trans. Wireless Commun.*, vol. 19, no. 2, pp. 1305-1319, Feb. 2020.

[13] Y. Chen, N. Zhao, Z. Ding, and M. Alouini, "Multiple UAVs as relays: Multi-hop single link versus multiple dual-hop links," *IEEE Trans. Wireless Commun.*, vol. 17, no. 9, pp. 6348-6359, Sep. 2018.

[14] Y. Zeng, J. Lyu and R. Zhang, "Cellular-Connected UAV: Potential, challenges, and promising technologies," *IEEE Wireless Commun.*, vol. 26, no. 1, pp. 120-127, Feb 2019.

[15] R. Amer, W. Saad, and N. Marchetti, "Mobility in the sky: Performance and mobility analysis for cellular-connected UAVs," *IEEE Trans. Commun.*, vol. 68, no. 5, pp. 3229-3246, May 2020.

[16] S. Zhang and R. Zhang, "Trajectory optimization for cellular-connected UAV under outage duration constraint," *J. Commun. Inf. Netw.*, vol. 4, no. 4, pp. 55-71, Dec. 2019.

[17] F. Zhou, R. Hu, Z. Li, and Y. Wang, "Mobile edge computing in unmanned aerial vehicle networks," *IEEE Wireless Commun.*, vol. 27, no. 1, pp. 140-146, Feb. 2020.

[18] Q. Hu, Y. Cai, G. Yu, Z. Qin, M. Zhao, and G. Li, "Joint offloading and trajectory design for UAV-enabled mobile edge computing systems," *IEEE Internet Things J.*, vol. 6, no. 2, pp. 1879-1892, Apr. 2019.

[19] Y. Zeng, X. Xu, S. Jin, and R. Zhang, "Simultaneous navigation and radio mapping for cellular-connected UAV with deep reinforcement learning," *IEEE Wireless Commun.*, vol. 20, no. 7, pp. 4205 - 4220, Jul. 2021.

[20] Y. Zeng and R. Zhang, "Energy-Efficient UAV communication with trajectory optimization," *IEEE Trans. Wireless Commun.*, vol. 16, no. 6, pp. 3747-3760, Jun. 2017.

[21] X. Yuan, Y. Hu, J. Zhang, and A. Schmeink, "Joint user scheduling and UAV trajectory design on completion time minimization for UAV-aided data collection," *IEEE Trans. Wireless Commun.*, vol. 22, no. 6, pp. 3884-3898, Jun. 2023.

[22] M. Samir, S. Sharafeddine, C. Assi, T. Nguyen, and A. Ghrayeb, "UAV trajectory planning for data collection from time-constrained IoT devices," *IEEE Trans. Wireless Commun.*, vol. 19, no. 1, pp. 34-46, Jan. 2020.

[23] T. Feng, L. Xie, J. Yao, and J. Xu, "UAV-enabled data collection for wireless sensor networks with distributed beamforming," *IEEE Trans. Wireless Commun.*, vol. 21, no. 2, pp. 1347-1361, Feb. 2022.

[24] J. Liu, P. Tong, X. Wang, B. Bai, and H. Dai, "UAV-aided data collection for information freshness in wireless sensor networks," *IEEE Trans. Wireless Commun.*, vol. 20, no. 4, pp. 2368-2382, Apr. 2021.

[25] K. Nguyen, T. Duong, T. Do-Duy, H. Claussen, and L. Hanzo, "3D UAV trajectory and data collection optimisation via deep reinforcement learning," *IEEE Trans. Wireless Commun.*, vol. 70, no. 4, pp. 2358-2371, Apr. 2022.

[26] X. Li, S. Cheng, H. Ding, M. Pan, and N. Zhao, "When UAVs meet cognitive radio: Offloading traffic under uncertain spectrum environment via deep reinforcement learning," *IEEE Trans. Wireless Commun.*, vol. 22, no. 2, pp. 824-838, Feb. 2023.

[27] R. Beard and T. McLain, *Small Unmanned Aircraft: Theory and Practice*. Princeton University Press, 2012.

[28] K. Ogata, *Modern Control Engineering*. 5th edition, Prentice Hall, 2010.

[29] B. Li, Q. Li, Y. Zeng, Y. Rong, and R. Zhang, "3D trajectory optimization for energy-efficient UAV communication: A control design perspective," *IEEE Trans. Wireless Commun.*, vol. 21, no. 6, pp. 4579-4593, June. 2021.

[30] R. Mahony, V. Kumar, and P. Corke, "Multirotor aerial vehicles: Modeling, estimation, and control of quadrotor," *IEEE Robotics & Automation Magazine*, vol. 19, no. 3, pp. 20-32, Sep. 2012.

[31] A. Filippone, *Flight Performance of Fixed and Rotary Wing Aircraft*. Washington DC, USA: AIAA, 2006.

[32] J. Liu and H. Zhang, "Height-Fixed UAV enabled energy-efficient data collection in RIS-aided wireless sensor networks," *IEEE Trans. Wireless Commun.*, vol. 22, no. 11, pp. 7452-7463, Nov. 2023.

[33] Y. Zeng, J. Xu, and R. Zhang, "Energy minimization for wireless communication with rotary-wing UAV," *IEEE Trans. Wireless Commun.*, vol. 18, no. 4, pp. 2329-2345, Apr. 2019.

[34] Y. Zhang, J. Lyu, and L. Fu, "Energy-efficient trajectory design for UAV-aided maritime data collection in wind," *IEEE Trans. Wireless Commun.*, vol. 21, no. 12, pp. 10871-10886, Dec. 2022.

[35] H. Yang, Y. Ye, X. Chu, and S. Sun, "Energy efficiency maximization for UAV-enabled hybrid backscatter-harvest-then-transmit communications," *IEEE Trans. Wireless Commun.*, vol. 21, no. 5, pp. 2876-2891, May 2022.

[36] *Enhanced LTE Support for Aerial Vehicles*, Standard 3GPP TR 36.777, Jul. 2017. [Online]. Available: ftp://www.3gpp.org/specs/archive/36 series/36.777

[37] M. Dabiri, H. Safi, S. Parsaeefard, and W. Saad, "Analytical channel models for millimeter wave UAV networks under hovering fluctuations," *IEEE Trans. Wireless Commun.*, vol. 19, no. 4, pp. 2868-2883, Apr. 2020.

[38] F. T. Faul, D. Korthauer and T. F. Eibert, "Impact of Rotor Blade Rotation of UAVs on Electromagnetic Field Measurements," *IEEE Trans. Instrum Meas.*, vol. 70, pp. 1-9, Sept. 2021.

[39] Y. Zeng and R. Zhang. "Optimized Training Design for Wireless Energy Transfer," *IEEE Trans. Commun.*, vol. 63, no. 2, pp. 536-550, Feb. 2015.

[40] B. Li, C.J. Yu, K.L. Teo and G.R. Duan. "An exact penalty function method for continuous inequality constrained optimal control problem," *J. Optim. Theory Appl.*, vol. 151 no. 2, pp. 260-291, 2011.

[41] K. Teo, B. Li, C. Yu, and V. Rehbock, *Applied and Computational Optimal Control: A Control Parametrization Approach*. Cham, Switzerland: Springer, 2021.

Hongyun Zhang received the Master degree of science in operations research and cybernetics from Dalian University of Technology, China, in 2022. She is currently pursuing her Ph.D. degree in information and communication engineering from Sichuan University, China. Her research interests include sensing, communication and control co-design, and trajectory optimization.

Bin Li (M'18-SM'18) received the Bachelor degree in automation and the Master degree in control science and engineering from Harbin Institute of Technology, China, in 2005 and 2008, respectively, and Ph.D. degrees in mathematics and statistics from Curtin University, Australia, in 2011. From 2012-2014, he was a Research Associate with the School of Electrical, Electronic and Computer Engineering, the University of Western Australia, Australia. From 2014-2017, he was a Research Fellow with the Department of Mathematics and Statistics, Curtin University, Australia. Currently, he is a Professor with the School of Aeronautics and Astronautics, Sichuan University, China. His research interests include stochastic model predictive control, optimal control, optimization, signal processing, and wireless communications.
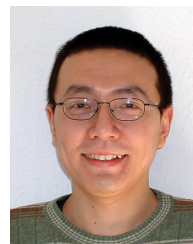
Yue Rong (Senior Member, IEEE) received the Ph.D. degree (summa cum laude) in electrical engineering from Darmstadt University of Technology, Darmstadt, Germany, in 2005. He was a Post-Doctoral Researcher with the Department of Electrical Engineering, University of California at Riverside, Riverside, CA, USA, from February 2006 to November 2007. Since December 2007, he has been with Curtin University, Bentley, WA, Australia, where he is currently a Professor. His research interests include signal processing for communications, underwater acoustic communications, underwater optical wireless communications, machine learning, speech recognition, and biomedical engineering. He has published over 200 journals and conference papers in these areas.

This article has been accepted for publication in IEEE Transactions on Communications. This is the author's version which has not been fully edited and content may change prior to final publication. Citation information: DOI 10.1109/TCOMM.2025.3543221

13

Yong Zeng (S'12-M'14-SM'22-F'25) is a Chief Young Professor with the National Mobile Communications Research Laboratory, Southeast University, China, and also with the Purple Mountain Laboratories, Nanjing, China. He received the Bachelor of Engineering (First-Class Honours) and Ph.D. degrees from Nanyang Technological University, Singapore. From 2013 to 2018, he was a Research Fellow and Senior Research Fellow at the Department of Electrical and Computer Engineering, National University of Singapore. From 2018 to 2019, he was a Lecturer at the School of Electrical and Information Engineering, the University of Sydney, Australia.

Prof. Zeng was listed as Highly Cited Researcher by Clarivate Analytics for six consecutive years (2019-2024). He is the recipient of the Australia Research Council (ARC) Discovery Early Career Researcher Award (DECRA), 2020 & 2024 IEEE Marconi Prize Paper Award in Wireless Communications, 2018 IEEE Communications Society Asia-Pacific Outstanding Young Researcher Award, 2020 & 2017 IEEE Communications Society Heinrich Hertz Prize Paper Award, 2021 IEEE ICC Best Paper Award, and 2021 China Communications Best Paper Award. He serves as an Editor for IEEE Transactions on Communications, IEEE Transactions on Mobile Computing, IEEE Communications Letters and IEEE Open Journal of Vehicular Technology, Leading Guest Editor for IEEE Wireless Communications on "Integrating UAVs into 5G and Beyond" and China Communications on "Network-Connected UAV Communications". He is the Symposium Chair for IEEE Globecom 2021 Track on Aerial Communications, the workshop co-chair for ICC 2018-2023 workshop on UAV communications, the tutorial speaker for Globecom 2018/2019 and ICC 2019 tutorials on UAV communications. Prof. Zeng proposed the concept of channel knowledge map (CKM) and the transmission method of delay-Doppler alignment modulation (DDAM). He has published more than 200 papers, which have been cited by more than 30,000 times based on Google Scholar. Prof. Zeng was elevated to IEEE Fellow "for contributions to unmanned aerial vehicle communications and wireless power transfer".

Rui Zhang (S'00-M'07-SM'15-F'17) received the B.Eng. (first-class Hons.) and M.Eng. degrees from the National University of Singapore, Singapore, and the Ph.D. degree from the Stanford University, Stanford, CA, USA, all in electrical engineering.

From 2007 to 2009, he worked as a researcher at the Institute for Infocomm Research, ASTAR, Singapore. In 2010, he joined the Department of Electrical and Computer Engineering of National University of Singapore, where he was appointed as the Provost's Chair Professor in 2020. He is currently with the School of Science and Engineering, Shenzhen Research Institute of Big Data, The Chinese University of Hong Kong, Shenzhen, as a X. Q. Deng Presidential Chair Professor. He has published over 300 journal papers and over 200 conference papers. He has been listed as a Highly Cited Researcher by Thomson Reuters/Clarivate Analytics since 2015. His current research interests include UAV/satellite communications, wireless power transfer, intelligent reflecting surface, reconfigurable MIMO, radio mapping and optimization methods.